Strong electron-phonon coupling and bipolarons in Sb₂S₃

Yun Liu [*]

Institute of High Performance Computing (IHPC), Agency for Science, Technology and Research (A*STAR),
1 Fusionopolis Way, 16-16 Connexis, Singapore 138632, Republic of Singapore
and Cavendish Laboratory, University of Cambridge, Cambridge CB3 0HE, United Kingdom

Bartomeu Monserrat [†]

Cavendish Laboratory, University of Cambridge, Cambridge CB3 0HE, United Kingdom
and Department of Materials Science and Metallurgy, University of Cambridge, Cambridge CB3 0FS, United Kingdom

Julia Wiktor [‡]

Department of Physics, Chalmers University of Technology, SE-412 96 Gothenburg, Sweden

Antimony sulfide (Sb₂S₃) is an Earth-abundant and nontoxic material that is under investigation for solar energy conversion applications. However, it still suffers from poor power conversion efficiency and a large open circuit voltage loss that have usually been attributed to point or interfacial defects. More recently, there has been some discussion in the literature about the role of carrier trapping in the optical properties of Sb₂S₃, with some reporting self-trapped excitons as the microscopic origin for the performance loss, while others have found no evidence of carrier trapping with only large polarons existing in Sb₂S₃. By using first-principles methods, we demonstrate that Sb₂S₃ exhibits strong electron-phonon coupling, a prerequisite for carrier self-trapping in semiconductors, which results in a large renormalization of 200 meV of the absorption edge when temperature increases from 10 to 300 K. When two electrons or holes are added to the system, corresponding to a carrier density of 1.6×10^{20} cm^{-3}, we find wave function localization consistent with the presence of bipolarons accompanying a significant lattice distortion with the formation of Sb and S dimers. The formation energies of the electron and hole bipolarons are -330 and -280 meV per carrier, respectively. Our results reconcile some of the controversy in the literature regarding carrier trapping in Sb₂S₃ and demonstrate the existence of large electron-phonon coupling and carrier self-trapping that might place a fundamental limit on the open circuit voltage and, consequently, the maximum efficiency of the photovoltaic cells.

I. INTRODUCTION

Photovoltaic (PV) solar cells are one of the key technologies for realizing a decarbonized economy as the Sun is an inexhaustible and clean energy source. Mainstream solar panels have been mainly based on crystalline silicon, which offers high power conversion efficiencies (PCEs) of over 25%, and their cost has decreased substantially over the years [1]. While other emerging materials such as organic-inorganic hybrid perovskites and thin film technologies such as copper indium gallium selenide (CIGS) and CdTe are making rapid improvements in PCEs, they still face stability, toxicity, and material scarcity issues [2]. To further increase the PCE and lower the cost of PV-generated electricity, tandem solar cells show great potential as they can break the Shockley-Queisser limit of single-junction solar cells [3]. The widely used silicon PV has a band gap of around 1.1 eV and is an ideal material for the bottom cell to absorb the lower-energy part of the solar spectrum. The search for top cell materials compatible with crystalline silicon is an active area of research for the scientific and engineering communities, with candidates ranging from III-V semiconductors to perovskites [4].

Among the many novel material candidates, the metal chalcogenide family has received a lot of attention due to their Earth-abundant and low-toxicity elements [5–8]. They also possess desirable band gaps and relatively benign synthesis conditions. In particular, antimony sulfide (Sb₂S₃) has a high absorption coefficient in the visible region and a band gap of 1.7 eV that is ideal for the top subcell in a Si-based tandem solar cell. Despite these promising traits, the record PCE of Sb₂S₃ is only about 7.5% [9], far from the minimum 18% needed for an efficient top cell [10]. This is due to the fact that Sb₂S₃ suffers from high open circuit voltage V_{oc} losses, even though the internal quantum efficiency is near unity and

[*]liu_yun@ihpc.a-star.edu.sg
[†]bm418@cam.ac.uk
[‡]julia.wiktor@chalmers.se

the fill factor is up to 70%. Irrespective of fabrication methods, the V_{oc} deficit corresponds to a potential energy drop of about 0.7 eV, half of the theoretical maximum allowed by its band gap. More recently, alloying and band gap tuning Sb_2S_3 with Sb_2Se_2 have increased the PCE of metal chalcogenide solar cells to a record of 10.7% [11]. This champion device's V_{oc} remains largely unchanged, with the PCE increase mainly coming from improvements in the short-circuit current and fill factor. The large V_{oc} loss has generally been ascribed to the presence of localized point defects such as sulfur vacancies or interfacial defects between Sb_2S_3 and the carrier transport layers [12–15]. Such trap states in the band gap can act as nonradiative recombination centers to reduce photocarrier populations [16]. Defects can also reduce the quasi-Fermi level splitting range under illumination and lead to lower V_{oc} and poor device performance.

Some recent reports have attributed the V_{oc} loss in metal chalcogenides to intrinsic carrier self-trapping [17–19]. In Sb_2S_3, the role of extrinsic defects was excluded by the observation of a few picosecond carrier trapping without saturation at a high carrier density of 10^{20} cm^{-3} and the polarized nature of trap emission from single crystals [17]. In Sb_2Se_3, lattice anharmonicity was observed with a 20 ps barrierless intrinsic self-trapping with associated polaronic lattice distortion [19]. On the other hand, a first-principles study found moderate Fröhlich coupling constants in these systems, and polarons having rather large radii extending over several unit cells [20]. Furthermore, the electrons and holes exhibit moderate mobilities in the range of 1–10 cm^2 V^{-1} s^{-1}, showing that transport might be bandlike or dominated by large polarons [21–23]. Therefore, the debate on the role of small localized polaron and carrier trapping in Sb_2S_3 remains open.

A prerequisite for the formation of polarons is strong coupling between carriers and the lattice. Experimentally, the importance of electron-phonon coupling in Sb_2S_3 was studied by Chong and coworkers, who observed coherent phonon generation in pump-probe experiments and assigned it to the B_{3g} longitudinal optical phonon mode at 65 cm^{-1} [24]. It was also reported that an A_g optical phonon mode at 194 cm^{-1} is responsible for the excited state relaxation in Sb_2Se_3 [19]. The electronic structure and band gaps of Sb_2S_3 were also calculated at various levels of theory [25–27], and separately, the phonon dispersion and anisotropic thermal expansion were calculated [28,29]. However, a full microscopic characterization of electron-phonon coupling is still missing.

In this work, we perform a systematic first-principles study of electron-phonon coupling and polarons in Sb_2S_3. We reveal the presence of strong electron-phonon coupling, leading to a large absorption edge renormalization of 200 meV when temperature increases from 10 to 300 K. We find that there are negligible structural distortions when an electron is added or removed from the supercell with the charge density remaining delocalized across the system. In the presence of two excess electrons or holes per supercell, corresponding to a carrier density of 10^{20} cm^{-3}, we observe bipolarons associated with the formation of antimony and sulfur dimers, respectively. Our results contribute to the debate regarding the existence and role of polarons and highlight the complex carrier self-trapping properties in metal chalcogenide systems mediated by strong electron-phonon coupling.

II. METHODS

All density functional theory (DFT) calculations are performed using the Vienna Ab initio Simulation Package (VASP, version 5.4) [30,31]. The core-valence interaction is described using the projector augmented wave method [32], with five valence electrons for Sb ($5s^25p^3$) and six valence electrons for S ($3s^23p^4$). The electronic wave functions are expanded in a plane wave basis with an energy cutoff of 400 eV, and the Brillouin zone is sampled with a $12 \times 4 \times 12$ Γ-centered Monkhorst-Pack [33] **k**-point grid, with commensurate grids for the supercells. The atoms are relaxed until the Hellman-Feynman force converges below 10^{-2} eV Å^{-1}, and the volume is relaxed until all components of the stress tensor are below 10^{-2} GPa.

All phonon dispersions are computed using the finite-displacement method with a $2 \times 6 \times 2$ supercell containing 480 atoms ($22.6 \times 23.2 \times 22.1$ Å^3) as implemented in the PHONOPY package [34]. For phonon dispersions, a nonanalytical term is added to the dynamical matrix to treat the long-range interaction arising from the macroscopic electric field induced by the polarization of collective ionic motions near Γ [35].

To include the effects of electron-phonon interactions on optical absorption at a given temperature T, we evaluate the imaginary part of the frequency-dependent dielectric function $\varepsilon_2(\omega, T)$ within the independent particle approximation using the Williams-Lax theory:

$$\varepsilon_2(\omega, T) = \frac{1}{\mathcal{Z}} \sum_{\mathbf{s}} \langle \Phi_{\mathbf{s}}(\mathbf{u}) | \varepsilon_2(\omega, T) | \Phi_{\mathbf{s}}(\mathbf{u}) \rangle \, e^{-E_{\mathbf{s}}/k_B T}, \quad (1)$$

where $\Phi_{\mathbf{s}}$ is the vibrational wave function in state $\mathbf{s}$ with energy $E_{\mathbf{s}}$, evaluated within the harmonic approximation, and $\mathcal{Z} = \sum_{\mathbf{s}} e^{-E_{\mathbf{s}}/k_B T}$ is the partition function, where k_B is Boltzmann's constant. For these calculations, we recompute the phonon frequencies and eigenvectors using nondiagonal supercells [36] and then use them as a starting point to evaluate Eq. (1) with Monte Carlo integration accelerated by thermal lines [37,38].

From the finite-temperature dielectric function, the absorption coefficient is given by $\alpha(\omega) = \frac{\omega}{cn(\omega)} \varepsilon_2(\omega)$, where c is the speed of light in vacuum, $\varepsilon_2(\omega)$ is the imaginary part of the dielectric function, and $n(\omega)$ is the real part of the complex refractive index. $n^2(\omega) = \frac{1}{2}(\varepsilon_1 + \sqrt{\varepsilon_2^2 + \varepsilon_1^2})$, where $\varepsilon_1(\omega)$ is the real part of the dielectric function. $\varepsilon_1(\omega)$ is obtained from $\varepsilon_2(\omega)$ through the Kramers-Kronig relation. Convergence tests show that a $2 \times 6 \times 2$ supercell and a $2 \times 2 \times 2$ electronic **k** grid lead to accurate results, with the tetrahedron smearing method [39] and small complex shift (10^{-6}) in the Kramers-Kronig transformation.

For the fulfillment of the Koopmans's condition, the corrections to the unoccupied Kohn-Sham eigenvalues of the defect-induced single-particle levels are calculated as [40]

$$\epsilon_{corr}^{KS} = \frac{-2}{q} E_{corr}, \quad (2)$$

where q is the charge of the defect and E_{corr} is the finite-size electrostatic correction. E_{corr} is computed using SXDEFECTAL-IGN [41] with an anisotropic screening where the diagonal
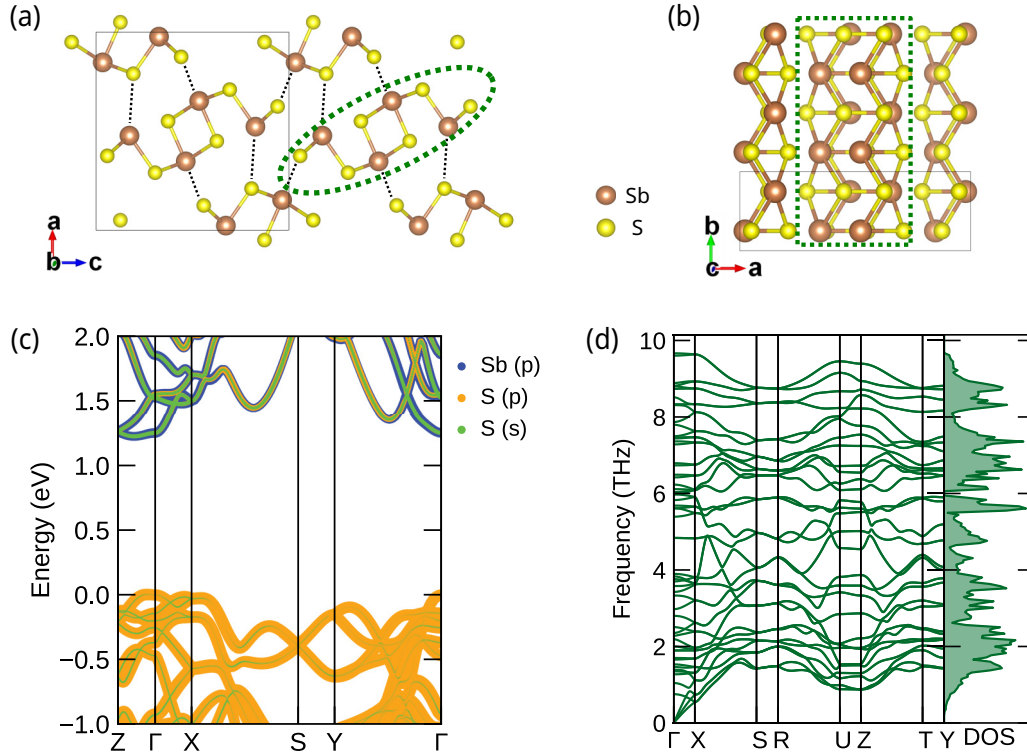
FIG. 1. (a) Sb_2S_3 crystal structure viewed from the [010] axis, with the unit cell enclosed by the black box. Brown and yellow spheres represent Sb and S atoms, respectively. One $[Sb_4S_6]$ ribbon is encircled by the green dashed line. The intraribbon bonds are indicated by the solid brown-yellow lines, and the interribbon van der Waals interactions are indicated by black dashed lines. (b) Sb_2S_3 crystal structure viewed from the [001] axis, with the ribbon enclosed in a green dashed box. (c) The projected band structures along high-symmetry lines of the Brillouin zone calculated at the optB86b level, with the orbital contributions drawn as a series of stacked circles. (d) The phonon dispersion of Sb_2S_3 along high-symmetry lines of the Brillouin zone, with the total phonon density of states in the right panel.

terms of the high-frequency dielectric tensor are $\varepsilon_{xx} = 11$, $\varepsilon_{yy} = 8$, and $\varepsilon_{zz} = 12$ [42].

For polaron and bipolaron calculations, we use a $2 \times 6 \times 2$ supercell to minimize spurious interactions between periodic images and sample only the Γ point. After the addition or removal of an electron from the supercell, structural relaxation is performed using spin-polarized calculations in which the supercell lattice parameters are fixed and the atoms allowed to move, with the same force convergence criterion of 10^{-2} eV Å^{-1}. The bipolaron is set in the singlet (S0) state, which is lower in energy than the triplet (T1) state by 1.65 eV. The binding energy of the electron or hole bipolaron per electron E_p can be estimated using the following formula for defect formation energy calculations [43]:

$$E_p = \frac{E_q[\text{bipolaron}] - E[\text{pristine}] + 2qE_{\text{edge}} + E_{\text{corr}}}{2}, \quad (3)$$

where $E_q[\text{bipolaron}]$ is the total energy of the distorted supercell of the bipolaronic state; $E[\text{pristine}]$ is the total energy of the perfect crystal using an equivalent supercell, with q denoting the excess of charge of an electron or hole; and E_{edge} is the energetic position of the conduction band minimum (CBM) or valence band maximum (VBM). The diagonal components of the static dielectric tensor are used with $\varepsilon_{xx} = 94$, $\varepsilon_{yy} = 13$, and $\varepsilon_{zz} = 99$ [42].

Crystal structures and isosurfaces are visualized using VESTA [44], and graphs are plotted by SUMO [45] and custom scripts.

III. RESULTS AND DISCUSSION

A. Equilibrium properties

The orthorhombic phase of Sb_2S_3 belongs to the space group *Pbnm* with 20 atoms per unit cell. Its crystal structure is highly anisotropic with covalently bonded one-dimensional (1D) ribbons of $[Sb_4S_6]$ along the [010] or b direction [Figs. 1(a) and 1(b)]. These ribbons are, in turn, weakly bonded in a zigzag fashion in the (010) plane by van der Waals (vdW) interactions. Due to the presence of vdW interactions, we test the nonlocal vdW density functional (vdW-DF), optimized vdW functional with Becke 86 exchange (optB86b) and strongly constrained and appropriately normed (SCAN) with revised-Vydrov and Van Voorhis dispersions (SCAN + rVV10) [47,48], against some commonly used semilocal, meta-generalized gradient approximation (metaGGA) and hybrid functionals [49–52] (details are given in the Sec. II). While most functionals are able to reproduce the b lattice parameter accurately, the vdW functional performs the best at simultaneously reproducing a and c accurately (see Table I). There are little differences in the calculated lattice parameter between the optB86b and SCAN + rVV10 functionals.

TABLE I. The lattice parameters and band gaps of Sb_2S_3 calculated using different DFT exchange-correlation functionals and compared with experimental values [46].

	Lattice parameter (Å)				
	a	b	c	E_g^{direct}	E_g^{indirect}
optB86b	11.324	3.865	11.053	1.241	1.228
SCAN + rVV10	11.315	3.843	11.085	1.362	1.362
SCAN	11.672	3.847	11.254	1.382	1.382
PBE	12.170	3.870	11.228	1.259	1.241
PBEsol	11.267	3.829	10.908	1.307	1.287
HSE06	12.081	3.802	11.389	1.745	1.740
Experiment	11.311	3.836	11.229	1.7	

We then compute the orbital-projected band structure, which is plotted in Fig. 1(c). The VBM consists of mainly S $3p$ orbitals, and the CBM is dominated by Sb-S bonds made up of Sb $5p$ and S $3s$ orbitals. The positions of the VBM and CBM are located slightly away from Γ at (0,0,0.103) and (0,0,0.282), respectively. This means that Sb_2S_3 is an indirect band gap semiconductor, which was reported by previous theoretical studies [27] and experimentally observed in low-temperature optical measurements by Fujita and coworkers [53].

The vdW functional suffers from the same self-interaction error as other semilocal and metaGGA functionals and underestimates the band gap to be around 1.24 eV (Table I). Using the hybrid functional of Heyd, Scuseria, and Ernzerhof (HSE06) leads to a direct band gap of 1.75 eV that is close to the experimental value. Our results are in general agreement with previously calculated band gaps in the range of 1.2–1.7 eV at different levels of theory [25–27]. Due to the small difference between direct and indirect band gaps, $\Delta(E_g^{\text{direct}} - E_g^{\text{indirect}}) < 20$ meV, Sb_2S_3 is often treated as an effective direct band gap semiconductor. While hybrid functionals can more accurately reproduce the band gap, the computational cost is significantly larger than that of metaGGA functionals like SCAN + rVV10, which in turn has higher computational cost than optB86b. We therefore use the optB86b functional for the electron-phonon calculations in this study and apply a HSE06-derived scissor shift to the band gaps when necessary. The computed phonon dispersion and density of states (DOS) is shown in Fig. 1(d), which exhibits no imaginary modes, indicating dynamical stability.

For polaron calculations, hybrid functionals are necessary to describe the charge localization [54–56]. To determine the fraction of Fock exchange needed to cancel the self-interaction error, we verify the fulfillment of the Koopmans's condition of the screened hybrid functional. This is done by calculating the occupied and unoccupied single-particle energy levels related to the +/0 transition of an unrelaxed sulfur vacancy, which lies within the semiconductor gap of Sb_2S_3 [57]. We vary the amount of exact Fock exchange while keeping the screening parameter constant at 0.2. Figure S1 in the Supplemental Material shows the computed band edges and the energy levels for the sulfur vacancy transitions [58]. We note that the single-particle energy levels shown in Fig. S1 include finite-size corrections [41,59,60]. The crossing between the levels calculated in the 0 and +1 charges of the

supercell corresponds to the value of exact exchange for which the Koopmans's condition is satisfied. As this crossing value of 0.24 is very close to the default value of 0.25 in HSE06, we use the default 0.25 Fock exchange for the subsequent polaron calculations.

B. Temperature-dependent structural and optical properties

The first effect we consider for the description of the finite-temperature optoelectronic properties of Sb_2S_3 is the role of thermal expansion. Using the quasiharmonic approximation (QHA) [61], we consider primitive cell volumes ranging from 483.5 to about 502 Å³ in 15 equidistant steps. As the unit cell of Sb_2S_3 is orthorhombic, the lattice parameters and atomic positions at each volumetric step are relaxed while keeping the volume constant. Then the Helmholtz free energies of the relaxed structures are calculated within the harmonic approximation of the lattice dynamics. Figure 2(a) depicts the Helmholtz free energy relative to the static lattice energy as a function of lattice volume for temperatures ranging from 0 to 400 K. The minimum of each fitted free-energy curve gives the quasiharmonic volume at the corresponding temperature. The zero-point quantum motion contributes a volume increase of about 2 Å³, and thermal expansion increases the volume by an additional 7.5 Å³ in the studied temperature range.

Figure 2(b) shows a comparison between the experimental temperature-dependent volume [62] and the QHA results. The raw DFT calculations overestimate the volume by a constant 2.5 Å³ from 128 to 293 K, where experimental data are available, which is mainly due to the accuracy limits of the optB86b functional. There is remarkable agreement between theory and experiment if this systematic error is corrected, revealing that thermal expansion is correctly captured by our model.

Both E_g^{direct} and E_g^{indirect} change by about 9 meV when we consider the influence of thermal expansion from 0 to 400 K. This change is negligible compared to the absorption edge renormalization induced by electron-phonon coupling, which will be discussed next. Therefore, we will ignore the effects of thermal expansion in the rest of this work.

Figure 2(c) shows the absorption spectrum of Sb_2S_3 in logarithmic scale calculated with the optB86b functional and a HSE06-derived scissor correction. The absorption onset at 10 K is about 100 meV below that of the static level, indicating the importance of zero-point motion. Increasing temperature leads to a further redshift of the absorption onset, a result that is consistent with recent experimental measurements of Bi_2S_3 in the chalcogenide family [64]. The calculated absorption onset changes by around 200 meV from 10 to 300 K, somewhat larger than the value of 159 meV reported for Bi_2S_3, but the difference likely arises from the mass difference between Bi and Sb [63]. Absorption onset redshifts of about 100 meV have been observed in other conventional III-V and van der Waals semiconductors (see Table II).

The large redshift in the temperature-dependent absorption onset shows that Sb_2S_3 exhibits large electron-phonon coupling. Such strong coupling between electrons and phonons provides the necessary conditions for the possible generation of small localized polarons, which we discuss next.
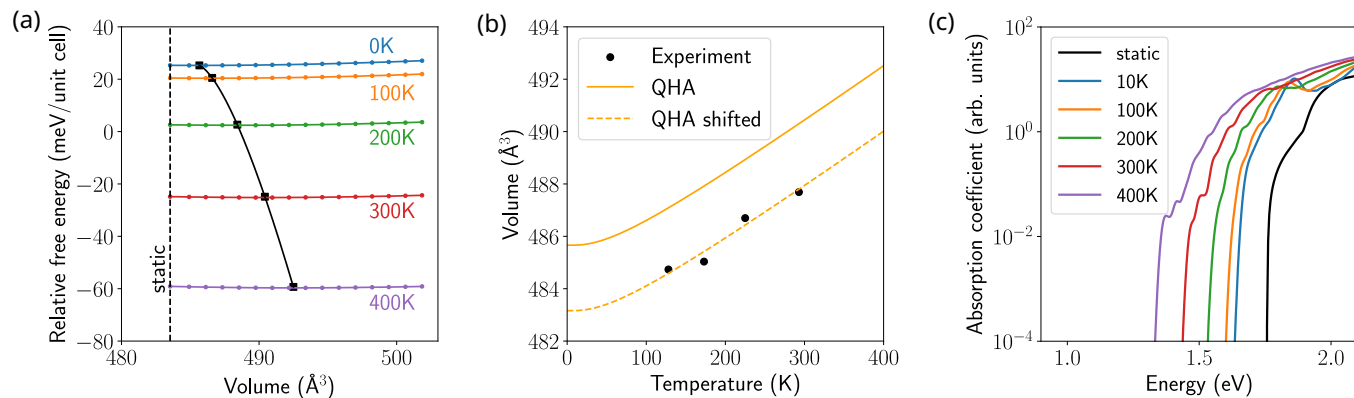
FIG. 2. (a) Relative Helmholtz free energy as a function of the unit cell volume for temperatures between 0 and 400 K. The black dashed vertical line indicates the volume at the static DFT level, and the black squares indicate the minima of fitted free-energy curves at each given temperature with the Rose-Vinet equation of state. (b) The unit cell volume as a function of temperature as calculated by the QHA. The QHA data are also shifted by $-2.5\,\text{Å}^3$ to guide the comparison with experimental volumes [62]. (c) Absorption coefficient at temperatures from 10 to 400 K including phonon-assisted processes. A scissor operator of 0.5 eV is applied to all the spectra to align the static DFT band gap to the HSE06 level.

C. Carrier trapping

The evidence of carrier self-trapping was supported by transient absorption measurements on Sb_2S_3 which showed that the populations of the trapped carriers do not exhibit any saturation at a high carrier density of $10^{20}\,\text{cm}^{-3}$, implying that trapping is not due to defects because their concentrations were measured to be small in the same studies [17,19]. More evidence is provided by the polarized PL emission. It was argued that it can arise only from the preferred dipole alignment of the self-trapped carriers, ruling out the role of defects, which are typically randomly distributed. However, other studies reported significantly larger defect densities [68,69] and that defect-trapped charges can also induce a preferred dipole alignment in some ferroelectrics [70]. The experimental results supporting self-trapping can therefore also be explained by the presence of defects. Furthermore, a first-principles study found that polarons in Sb_2S_3 and Sb_2Se_3 have large radii extending over several unit cells with moderate Fröhlich coupling constants [20]. Small polarons and therefore carrier self-trapping are unlikely to occur.

To resolve some of these controversies, we perform a systematic investigation of the polarons and bipolarons using a large $2 \times 6 \times 2$ supercell with 480 atoms. To find the polaronic geometry, we apply the bond distortion method to various bonds to break the symmetry of the crystal structure [71], which was shown to lead to faster convergence by mimicking the experimentally observed polaronic distortions. One excess electron is then added or removed from the su-

percell, and the atomic positions are relaxed (see details in Sec. II). We find that there is little resultant structural distortion, with few changes in the wave functions of the CBM and VBM states, as shown in Fig. S2 [58]. The excess electron is delocalized over the Sb atoms located on the edges of a $[Sb_4S_6]$ ribbon, while the excess hole is delocalized over the entire supercell. Due to the delocalized nature of the band edge wave function, the formation energy of the excess carrier is calculated as the difference between the total energy of the supercell before and after structural relaxation. The formation energy of 4 meV is within the error of the DFT method and well below the energy of thermal fluctuations at room temperature, meaning that the formation of a small polaron is unlikely. These results are in agreement with the conclusions reached in the work of Wang *et al.* [20].
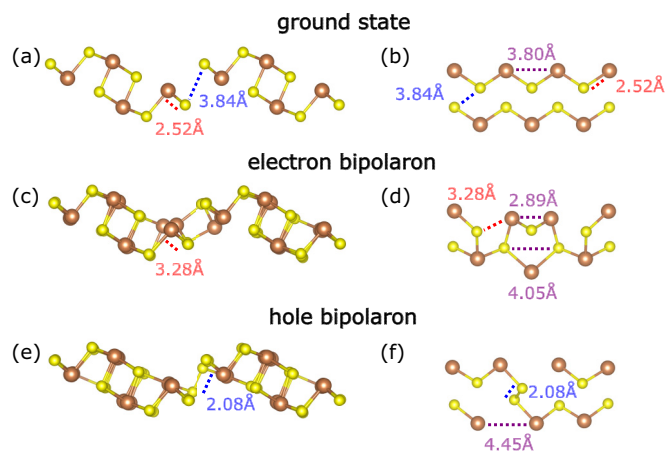
TABLE II. The change in band gap for selected semiconductors in the temperature range from 10 to 300 K.

Material	ΔE_g (meV)	Reference
Sb_2S_3	200	This study
Bi_2S_3	159	[64]
GaAs	96	[65]
GaSb	85	[65]
MoS_2	95	[66]
WSe_2	66	[67]

FIG. 3. Bond distortions arising from excess electrons and holes. (a) and (b) The crystal structure and selected bond lengths of ground state Sb_2S_3, with characteristic interchain S-S (blue) and intrachain Sb-Sb (purple) and Sb-S (red) distances. (c) and (d) Distorted structures in the presence of an electron bipolaron, with Sb-Sb antimony dimer bond lengths at 2.89 Å. (e) and (f) Distorted structures in the presence of a hole bipolaron, with S-S sulfur dimer bond lengths at 2.08 Å.
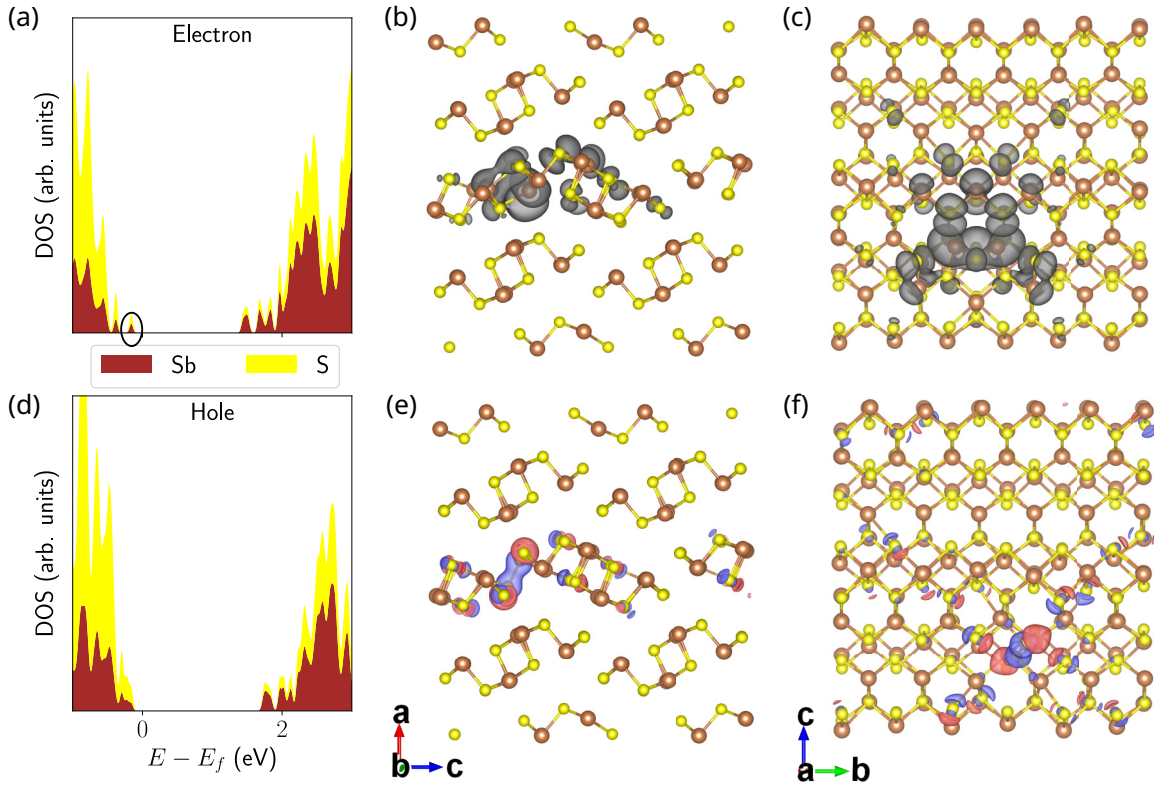
FIG. 4. Electronic structures of the polaronic states. (a) and (d) Projected density of states (PDOS) of the relaxed bipolaronic structures with two excess electrons and holes, respectively. The energetic locations of the electron bipolaron and hole bipolaron states are circled. (b) and (c) Wave function isosurface of the electron bipolaron as viewed from the b and c axes. (e) and (f) The difference between the total charge density of the hole bipolaron and the pristine Sb_2S_3 as viewed from the b and c axes. Blue and red represent positive and negative values.

We next investigate the addition or removal of two excess electrons, or bipolarons, which have been investigated in conjugated polymers and oxides for their role in magnetoresistance and transport properties [72–74]. Like in the search for polaronic structure, two excess electrons are added or removed from the supercell, and the atomic positions are relaxed after applying the bond distortion method. We note that the resultant excited carrier density of $1.6 \times 10^{20} \, \mathrm{cm}^{-3}$ is of the same order of magnitude as the carrier densities used in the transient absorption spectroscopy measurements of Sb_2S_3 [17]. Compared with the ground state geometry [Figs. 3(a) and 3(b)], there is a significant structural distortion with the elongation of the typical Sb-S bond from 2.52 to 3.28 Å with two excess electrons [Fig. 3(c)]. Within the $[Sb_4S_6]$ chain, antimony dimers form, with the nearest Sb-Sb distance decreasing from 3.80 to 2.89 Å, while the S-S distance increases from 3.80 to 4.05 Å [Fig. 3(d)]. Dimer formation in the presence of bipolarons has been observed in oxides such as TiO_2, $LiNbO_3$, and $BiVO_4$ [75–77]. The dimer formation can be understood from energetics: if the energy gained from the formation of the bonding orbitals between the antimony atoms is larger than the Coulomb repulsion between the two excess electrons, the two electron polarons can bind with each other and induce dimerization [76]. The electron bipolaron state appears at the top of the valence bands [Fig. 4(a)], with its wave function localized between two $[Sb_4S_6]$ chains near the antimony dimers [Figs. 4(b) and 4(c)].

Analogously, the introduction of two excess holes results in the formation of a sulfur dimer between two neighboring $[Sb_4S_6]$ chains, with the S-S distance decreasing from 3.84 to 2.08 Å [Figs. 3(e) and 3(f)]. The formation of the sulfur dimer pushes the state associated with its two holes far into the conduction band [Fig. 4(d)], where hybridization with conduction states occurs [76,77]. For this reason, it is impossible to isolate these two holes for visualization. For illustrative purposes, we plot the difference between the total charge density of the hole bipolaron and pristine Sb_2S_3 in Figs. 4(e) and 4(f), showing that the bonding orbitals exist between the two sulfur atoms in the dimer. By modifying the defect formation energy expression, we compute the formation energies per carrier for electron and hole bipolarons as -330 and -280 meV, respectively [Eq. (3)]. The presence of the localized bipolarons can result in a small redshifted shoulder peak in the absorption spectrum (Fig. S3 [58]) that can serve as a possible experimental signature.

IV. CONCLUSION

We found that the absorption edge of the quasi-1D semiconductor Sb_2S_3 redshifts by about 200 meV from 10 to 300 K, a higher value than the corresponding shift observed in most conventional and van der Waals semiconductors. This shows that there is significant electron-phonon coupling in the system, which can result in strong temperature dependence

of the Urbach tail [78]. At higher operating temperature in the field, photovoltaic solar cells based on Sb_2S_3 might exhibit larger V_{oc} losses, as the radiative recombination rate is reduced by the increased amount of electronic disorder [79].

We further investigated the possibility of polarons and bipolarons in a system mediated by strong electron-phonon coupling. In the presence of one excess carrier, we found that no small polarons are formed, in agreement with previous studies. With two excess carriers per supercell and corresponding carrier densities of 1.6×10^{20} cm^{-3}, electron and hole bipolarons can cause the formation of sulfur and antimony dimers with localized wave functions. Our results reconcile some of the conflicting reports on carrier trapping in Sb_2S_3 and show that intrinsic self-trapping can occur without the presence of defect states. The absence of trapping in the polaron and the presence of trapping in the bipolaron might yield strong concentration dependence of the trapping rate in transient excitation measurements, which should be investigated in future studies. The limit to the device V_{oc} and, consequently, the maximum achievable PCE might need to be carefully investigated as a function of solar irradiance. In conclusion, while strategies focusing on improving material synthesis and processing conditions to reduce defects and interfacial losses can still increase the PCE, the maximum efficiency might never reach the 18% needed for the top cell in a tandem structure with silicon PV.

The VASP input and structure files for the ground state and bipolarons are available from Zenodo [80].

[1] T. Saga, Advances in crystalline silicon solar cell technology for industrial mass production, NPG Asia Mater. **2**, 96 (2010).

[2] J. Jean, P. R. Brown, R. L. Jaffe, T. Buonassisi, and V. Bulovic, Pathways for solar photovoltaics, Energy Environ. Sci. **8**, 1200 (2015).

[3] B. Ehrler, E. Alarcón-Lladó, S. W. Tabernig, T. Veeken, E. C. Garnett, and A. Polman, Photovoltaics reaching for the Shockley-Queisser limit, ACS Energy Lett. **5**, 3029 (2020).

[4] H. Li and W. Zhang, Perovskite tandem solar cells: From fundamentals to commercial deployment, Chem. Rev. **120**, 9835 (2020).

[5] D.-H. Kim, S.-J. Lee, M. S. Park, J.-K. Kang, J. H. Heo, S. H. Im, and S.-J. Sung, Highly reproducible planar Sb_2S_3-sensitized solar cells based on atomic layer deposition, Nanoscale **6**, 14549 (2014).

[6] L. Wang, D.-B. Li, K. Li, C. Chen, H.-X. Deng, L. Gao, Y. Zhao, F. Jiang, L. Li, F. Huang, Y. He, H. Song, G. Niu, and J. Tang, Stable 6%-efficient Sb_2Se_3 solar cells with a ZnO buffer layer, Nat. Energy **2**, 17046 (2017).

[7] X. Wang, R. Tang, C. Wu, C. Zhu, and T. Chen, Development of antimony sulfide-selenide $Sb_2(S,Se)_3$-based solar cells, J. Energy Chem. **27**, 713 (2018).

[8] R. Kondrotas, C. Chen, and J. Tang, Sb_2S_3 solar cells, Joule **2**, 857 (2018).

[9] Y. C. Choi, D. U. Lee, J. H. Noh, E. K. Kim, and S. I. Seok, Highly improved Sb_2S_3 sensitized-inorganic-organic heterojunction solar cells and quantification of traps by deep-level transient spectroscopy, Adv. Funct. Mater. **24**, 3587 (2014).

[10] W. R. Rucker, E. G. Sukenik, S. G. Rizzie, and D. P. Birnie, Thin film absorber selection to pair with silicon for 1-sun tandem photovoltaics, Solar Energy **238**, 178 (2022).

[11] Y. Zhao, S. Wang, C. Jiang, C. Li, P. Xiao, R. Tang, J. Gong, G. Chen, T. Chen, J. Li, and X. Xiao, Regulating energy band alignment via alkaline metal fluoride assisted solution post-treatment enabling $Sb_2(S,Se)_3$ solar cells with 10.7% efficiency, Adv. Energy Mater. **12**, 2103015 (2022).

[12] A. Darga, D. Mencaraglia, C. Longeaud, T. J. Savenije, B. O'Regan, S. Bourdais, T. Muto, B. Delatouche, and G. Dennler, On charge carrier recombination in Sb_2S_3 and its implication for the performance of solar cells, J. Phys. Chem. C **117**, 20525 (2013).

[13] Z. Cai and S. Chen, Extrinsic dopants in quasi-one-dimensional photovoltaic semiconductor Sb_2S_3: A first-principles study, J. Appl. Phys. **127**, 183101 (2020).

[14] A. Maiti, S. Chatterjee, and A. J. Pal, Sulfur-vacancy passivation in solution-processed Sb_2S_3 thin films: Influence on photovoltaic interfaces, ACS Appl. Energy Mater. **3**, 810 (2020).

[15] W. Lian, C. Jiang, Y. Yin, R. Tang, G. Li, L. Zhang, B. Che, and T. Chen, Revealing composition and structure dependent deep-level defect in antimony trisulfide photovoltaics, Nat. Commun. **12**, 3260 (2021).

[16] X. Wang, S. R. Kavanagh, D. O. Scanlon, and A. Walsh, Four-electron negative-U vacancy defects in antimony selenide, arXiv:2302.04901.

[17] Z. Yang, X. Wang, Y. Chen, Z. Zheng, Z. Chen, W. Xu, W. Liu, Y. M. Yang, J. Zhao, T. Chen, and H. Zhu, Ultrafast self-trapping of photoexcited carriers sets the upper limit on antimony trisulfide photovoltaic devices, Nat. Commun. **10**, 4540 (2019).

[18] P. Martin, S. Guizard, P. Daguzan, G. Petite, P. D'Oliveira, P. Meynadier, and M. Perdrix, Subpicosecond study of carrier trapping dynamics in wide-band-gap crystals, Phys. Rev. B **55**, 5799 (1997).

[19] W. Tao, L. Zhu, K. Li, C. Chen, Y. Chen, Y. Li, X. Li, J. Tang, H. Shang, and H. Zhu, Coupled electronic and anharmonic structural dynamics for carrier self-trapping in photovoltaic antimony chalcogenides, Adv. Sci. **9**, 2202154 (2022).

[20] X. Wang, A. M. Ganose, S. R. Kavanagh, and A. Walsh, Band versus polaron: Charge transport in antimony chalcogenides, ACS Energy Lett. **7**, 2954 (2022).

[21] J. A. Christians, D. T. Leighton, and P. V. Kamat, Rate limiting interfacial hole transfer in Sb_2S_3 solid-state solar cells, Energy Environ. Sci. **7**, 1148 (2014).

[22] M. Liu, Y. Gong, Z. Li, M. Dou, and F. Wang, A green and facile hydrothermal approach for the synthesis of high-quality semiconducting Sb_2S_3 thin films, Appl. Surf. Sci. **387**, 790 (2016).

[23] U. Chalapathi, B. Poornaprakash, and S.-H. Park, Influence of post-deposition annealing temperature on the growth of chemically deposited Sb_2S_3 thin films, Superlattices Microstruct. **141**, 106500 (2020).

[24] W. K. Chong, G. Xing, Y. Liu, E. L. Gui, Q. Zhang, Q. Xiong, N. Mathews, C. K. Gan, and T. C. Sum, Direct measurement of coherent phonon dynamics in solution-processed stibnite thin films, Phys. Rev. B **90**, 035208 (2014).

[25] R. Caracas and X. Gonze, First-principles study of the electronic properties of A_2B_3 minerals, with A = Bi,Sb and B = S,Se, Phys. Chem. Miner. **32**, 295 (2005).

[26] T. Ben Nasr, H. Maghraoui-Meherzi, H. Ben Abdallah, and R. Bennaceur, Electronic structure and optical properties of Sb_2S_3 crystal, Phys. B (Amsterdam, Neth.) **406**, 287 (2011).

[27] M. R. Filip, C. E. Patrick, and F. Giustino, *GW* quasiparticle band structures of stibnite, antimonselite, bismuthinite, and guanajuatite, Phys. Rev. B **87**, 205125 (2013).

[28] Y. Liu, K. T. Eddie Chua, T. C. Sum, and C. K. Gan, First-principles study of the lattice dynamics of Sb_2S_3, Phys. Chem. Chem. Phys. **16**, 345 (2014).

[29] C. K. Gan, J. R. Soh, and Y. Liu, Large anharmonic effect and thermal expansion anisotropy of metal chalcogenides: The case of antimony sulfide, Phys. Rev. B **92**, 235202 (2015).

[30] G. Kresse and J. Furthmüller, Efficient iterative schemes for *ab initio* total-energy calculations using a plane-wave basis set, Phys. Rev. B **54**, 11169 (1996).

[31] G. Kresse and J. Furthmüller, Efficiency of *ab-initio* total energy calculations for metals and semiconductors using a plane-wave basis set, Comput. Mater. Sci. **6**, 15 (1996).

[32] P. E. Blöchl, Projector augmented-wave method, Phys. Rev. B **50**, 17953 (1994).

[33] H. J. Monkhorst and J. D. Pack, Special points for Brillouin-zone integrations, Phys. Rev. B **13**, 5188 (1976).

[34] A. Togo and I. Tanaka, First principles phonon calculations in materials science, Scr. Mater. **108**, 1 (2015).

[35] X. Gonze and C. Lee, Dynamical matrices, Born effective charges, dielectric permittivity tensors, and interatomic force constants from density-functional perturbation theory, Phys. Rev. B **55**, 10355 (1997).

[36] J. H. Lloyd-Williams and B. Monserrat, Lattice dynamics and electron-phonon coupling calculations using nondiagonal supercells, Phys. Rev. B **92**, 184301 (2015).

[37] B. Monserrat, Vibrational averages along thermal lines, Phys. Rev. B **93**, 014302 (2016).

[38] B. Monserrat, Electron-phonon coupling from finite differences, J. Phys.: Condens. Matter **30**, 083001 (2018).

[39] P. E. Blöchl, O. Jepsen, and O. K. Andersen, Improved tetrahedron method for Brillouin-zone integrations, Phys. Rev. B **49**, 16223 (1994).

[40] W. Chen and A. Pasquarello, Correspondence of defect energy levels in hybrid density functional theory and many-body perturbation theory, Phys. Rev. B **88**, 115104 (2013).

[41] C. Freysoldt, J. Neugebauer, and C. G. Van de Walle, Fully *Ab Initio* Finite-Size Corrections for Charged-Defect Supercell Calculations, Phys. Rev. Lett. **102**, 016402 (2009).

[42] X. Wang, Z. Li, S. R. Kavanagh, A. M. Ganose, and A. Walsh, Lone pair driven anisotropy in antimony chalcogenide semiconductors, Phys. Chem. Chem. Phys. **24**, 7195 (2022).

[43] C. Freysoldt, B. Grabowski, T. Hickel, J. Neugebauer, G. Kresse, A. Janotti, and C. G. Van de Walle, First-principles calculations for point defects in solids, Rev. Mod. Phys. **86**, 253 (2014).

[44] K. Momma and F. Izumi, *VESTA*: A three-dimensional visualization system for electronic and structural analysis, J. Appl. Crystallogr. **41**, 653 (2008).

[45] A. M. Ganose, A. J. Jackson, and D. O. Scanlon, Sumo: Command-line tools for plotting and analysis of periodic *ab initio* calculations, J. Open Source Software **3**, 717 (2018).

[46] P. Bayliss and W. Nowacki, Refinement of the crystal structure of stibnite, $Sb_2S_3^1$, Z. Kristallogr. **135**, 308 (1972).

[47] J. Klimeš, D. R. Bowler, and A. Michaelides, Van der Waals density functionals applied to solids, Phys. Rev. B **83**, 195131 (2011).

[48] H. Peng, Z.-H. Yang, J. P. Perdew, and J. Sun, Versatile van der Waals Density Functional Based on a Meta-Generalized Gradient Approximation, Phys. Rev. X **6**, 041005 (2016).

[49] J. P. Perdew, K. Burke, and M. Ernzerhof, Generalized Gradient Approximation Made Simple, Phys. Rev. Lett. **77**, 3865 (1996).

[50] J. Sun, R. C. Remsing, Y. Zhang, Z. Sun, A. Ruzsinszky, H. Peng, Z. Yang, A. Paul, U. Waghmare, X. Wu, M. L. Klein, and J. P. Perdew, Accurate first-principles structures and energies of diversely bonded systems from an efficient density functional, Nat. Chem. **8**, 831 (2016).

[51] J. P. Perdew, A. Ruzsinszky, G. I. Csonka, O. A. Vydrov, G. E. Scuseria, L. A. Constantin, X. Zhou, and K. Burke, Restoring the Density-Gradient Expansion for Exchange in Solids and Surfaces, Phys. Rev. Lett. **100**, 136406 (2008).

[52] J. Heyd, G. E. Scuseria, and M. Ernzerhof, Hybrid functionals based on a screened Coulomb potential, J. Chem. Phys. **118**, 8207 (2003).

[53] T. Fujita, K. Kurita, K. Takiyama, and T. Oda, The fundamental absorption edge and electronic structure in Sb_2S_3, J. Phys. Soc. Jpn. **56**, 3734 (1987).

[54] H. Ouhbi and J. Wiktor, Polaron formation and hopping in tantalate perovskite oxides: $NaTaO_3$ and $KTaO_3$, Phys. Rev. B **104**, 235158 (2021).

[55] A. Janotti, J. B. Varley, M. Choi, and C. G. Van de Walle, Vacancies and small polarons in $SrTiO_3$, Phys. Rev. B **90**, 085202 (2014).

[56] C. Spreafico and J. VandeVondele, The nature of excess electrons in anatase and rutile from hybrid DFT and RPA, Phys. Chem. Chem. Phys. **16**, 26144 (2014).

[57] Z. Cai, C.-M. Dai, and S. Chen, Intrinsic defect limit to the electrical conductivity and a two-step p-type doping strategy for overcoming the efficiency bottleneck of Sb_2S_3-based solar cells, Solar RRL **4**, 1900503 (2020).

[58] See Supplemental Material at http://link.aps.org/supplemental/10.1103/PhysRevMaterials.7.085401 for fulfilment of the Koopmans' condition, wave functions for excess electrons and holes, and the absorption spectrum of the electron bipolaron.

[59] S. Falletta, J. Wiktor, and A. Pasquarello, Finite-size corrections of defect energy levels involving ionic polarization, Phys. Rev. B **102**, 041115(R) (2020).

[60] Y. Kumagai and F. Oba, Electrostatics-based finite-size corrections for first-principles point defect calculations, Phys. Rev. B **89**, 195205 (2014).

[61] A. Togo, L. Chaput, I. Tanaka, and G. Hug, First-principles phonon calculations of thermal expansion in Ti_3SiC_2, Ti_3AlC_2, and Ti_3GeC_2, Phys. Rev. B **81**, 174301 (2010).

[62] A. Kyono, M. Kimata, M. Matsuhisa, Y. Miyashita, and K. Okamoto, Low-temperature crystal structures of stibnite implying orbital overlap of Sb_5S_2 inert pair electrons, Phys. Chem. Miner. **29**, 254 (2002).

[63] H. Shang, J. Zhao, and J. Yang, Assessment of the mass factor for the electron-phonon coupling in solids, J. Phys. Chem. C **125**, 6479 (2021).

[64] W. M. Linhart, S. J. Zelewski, P. Scharoch, F. Dybała, and R. Kudrawiec, Nesting-like band gap in bismuth sulfide Bi_2S_3, J. Mater. Chem. C **9**, 13733 (2021).

[65] I. Vurgaftman, J. R. Meyer, and L. R. Ram-Mohan, Band parameters for III-V compound semiconductors and their alloys, J. Appl. Phys. **89**, 5815 (2001).

[66] M. Sigiro, Y.-S. Huang, C.-H. Ho, Y.-C. Lin, and K. Suenaga, Influence of rhenium on the structural and optical properties of molybdenum disulfide, Jpn. J. Appl. Phys. **54**, 04DH05 (2015).

[67] A. Arora, M. Koperski, K. Nogajewski, J. Marcus, C. Faugeras, and M. Potemski, Excitonic resonances in thin films of WSe_2: From monolayer to bulk material, Nanoscale **7**, 10421 (2015).

[68] R. Tang, X. Wang, W. Lian, J. Huang, Q. Wei, M. Huang, Y. Yin, C. Jiang, S. Yang, G. Xing, S. Chen, C. Zhu, X. Hao, M. A. Green, and T. Chen, Hydrothermal deposition of antimony selenosulfide thin films enables solar cells with 10% efficiency, Nat. Energy **5**, 587 (2020).

[69] L. Zhang, W. Lian, X. Zhao, Y. Yin, T. Chen, and C. Zhu, Sb_2S_3 seed-mediated growth of low-defect Sb_2S_3 on a TiO_2 substrate for efficient solar cells, ACS Appl. Energy Mater. **3**, 12417 (2020).

[70] W. L. Warren, G. E. Pike, K. Vanheusden, D. Dimos, B. A. Tuttle, and J. Robertson, Defect-dipole alignment and tetragonal strain in ferroelectrics, J. Appl. Phys. **79**, 9250 (1996).

[71] T. D. Pham and N. A. Deskins, Efficient method for modeling polarons using electronic structure methods, J. Chem. Theory Comput. **16**, 5264 (2020).

[72] M. H. Cohen, E. N. Economou, and C. M. Soukoulis, Small-bipolaron formation, Phys. Rev. B **29**, 4496 (1984).

[73] W. Wagemans, F. L. Bloom, P. A. Bobbert, M. Wohlgenannt, and B. Koopmans, A two-site bipolaron model for organic magnetoresistance, J. Appl. Phys. **103**, 07F303 (2008).

[74] J. T. Devreese and A. S. Alexandrov, Fröhlich polaron and bipolaron: Recent developments, Rep. Prog. Phys. **72**, 066501 (2009).

[75] O. F. Schirmer, M. Imlau, C. Merschjann, and B. Schoke, Electron small polarons and bipolarons in $LiNbO_3$, J. Phys.: Condens. Matter **21**, 123201 (2009).

[76] S. Chen and L.-W. Wang, Double-hole-induced oxygen dimerization in transition metal oxides, Phys. Rev. B **89**, 014109 (2014).

[77] N. Österbacka, F. Ambrosio, and J. Wiktor, Charge localization in defective $BiVO_4$, J. Phys. Chem. C **126**, 2960 (2022).

[78] J. Zhu, Y. Xia, G. Li, S. Zhou, S. Wimmer, G. Springholz, A. Pashkin, M. Helm, and H. Schneider, Absorption edge, Urbach tail, and electron-phonon interactions in topological insulator Bi_2Se_3 and band insulator $(Bi_{0.89}In_{0.11})_2Se_3$, Appl. Phys. Lett. **114**, 162105 (2019).

[79] E. Ugur, M. Ledinský, T. G. Allen, J. Holovský, A. Vlk, and S. De Wolf, Life on the Urbach edge, J. Phys. Chem. Lett. **13**, 7702 (2022).

[80] Y. Liu, B. Monserrat, and J. Wiktor, dataset for "Strong electron-phonon coupling and bipolarons in Sb_2S_3", Version 1, Zenodo, 2023, doi: 10.5281/zenodo.8129218.